Electronic Research Archive

ERA, 33(9): 5638–5660.
DOI: 10.3934/era.2025251
Received: 17 July 2025
Revised: 30 August 2025
Accepted: 04 September 2025
Published: 18 September 2025

https://www.aimspress.com/journal/era

Research article

A novel ship image enhancement method based on fusion of parallel-series stochastic resonance model and multi-scale spiking neural networks

Di Wang[1], Yang Wang[2,*], Zonglian Wang[3], Jianhong Huang[1] and Xiaowen Xu[1]

[1] Westlake Institute for Optoelectronics, Hangzhou 311400, China
[2] College of Information Engineering, Taizhou University, Taizhou 225300, China
[3] College of Mechanical and Electrical Engineering, China Jiliang University, Hangzhou 310018, China

* **Correspondence:** Email: wy23912@gmail.com; Tel: +8618030203344.

Abstract: Ship imaging has an impact on the visual judgment of the steersman and influences ship navigation safety. Traditional image enhancement methods struggle under adverse conditions and fail to account for the physiological mechanisms of human visual perception. Therefore, a novel method was proposed to enhance ship imaging by combining a visual neural signal encoding mechanism (accomplished by multi-scale spiking neural networks) with a multi-scale frequency-domain stochastic resonance model. First, the noisy image is encoded by mapping the neuron pulse count per unit time, and then the encoded signal is directionally filtered by constructing a spatial dot-matrix dual-view perception receptive field model to achieve preliminary low-level noise reduction. Second, a stochastic resonance system is constructed and applied in series to enhance the decomposed multi-scale wavelet coefficients. Finally, considering the brightness characteristics of the visual system, the processed wavelet coefficients of each scale are inversely transformed and reconstructed. The reconstructed image is then fused with the image obtained by directional filtering of the spatial dot-matrix dual-view pathway receptive field model to produce the final enhanced image. According to the experimental results, compared with the original noisy image, the peak signal-to-noise ratio (PSNR) and visual information fidelity (VIF) improve by 27% and 30%, respectively. These findings indicate that the proposed method can effectively enhance ship images in a manner more consistent with the physiological characteristics of human visual imaging and signal processing.

Keywords: pulse coding; stochastic resonance; neural networks; image enhancement

1. Introduction

The quality of ship imaging plays an important role in ship navigation safety. However, when ships collect images during navigation, these are often affected by bad weather, interference from the equipment, dim light, etc. These factors result in an overall image that is noisy and dimly lit, which makes it hard to distinguish the details of the hull and affects visual judgment. Therefore, it is crucial to improve the quality of ship imaging to ensure the safety of ship navigation.

Several image enhancement methods have been proposed for dealing with noise or contrast issues. For example, Li and Duan proposed an improved bilateral filtering method combined with an adaptive threshold sliding window for enhancing shipping images with mixed noise [1]. Bai et al. proposed an infrared image contrast enhancement algorithm based on multi-scale new top-hat transformation for ship images in infrared imaging [2]. In this method, the multi-scale white and black new top-hat transformation is used to extract multi-scale bright and dark infrared image regions, which are used to construct the final bright and dark infrared regions for image enhancement. The contrast of the infrared image is enhanced through a power strategy. Román et al. proposed a multi-scale top-hat transformation based on reconstruction, which extracts multiple features from medical images for improving contrast brightness and displaying more details for image enhancement [3]. In [4], Pei et al. proposed a pseudo-transmittance model based on the principle of infrared radiation imaging to solve the problems of low contrast and blurry details in ocean infrared images. Besides, they also proposed an enhancement algorithm using morphological single-scale pseudo-transmittance modulation and radiation source enhancement. In [5], Gammaitoni et al. mentioned that neurons also have a stochastic resonance mechanism, which can remove the noise of one-dimensional signals. As a matter of fact, the stochastic resonance mechanism has positive effects in removing image noise and enhancing contrast. Therefore, Shi et al. proposed a parallel asymmetric stochastic resonance model to preprocess the electroencephalogram (EEG) images by a convolutional neural network (CNN) classifier [6], which can not only avoid the loss of information of EEG but also provide a CNN with high-quality EEG of diversified frequency information to enhance its performance. A general method for reconstructing images through seed instability was proposed in [7], and the predicted but not yet observed information limitations in nonlinear communication systems were confirmed. Moreover, the application of the stochastic resonance mechanism by Liao et al. achieved innovative breakthroughs in one-dimensional signals. For example, in [8], they proposed a robust QRS detection method based on a stochastic resonance one-dimensional lattice potential for noisy electrocardiograms, which can improve the noise margin for maintaining optimal performance. In [9], the authors adopted some common suppressed graphs in SuiteSparse Matrix Collection as MAXCUT benchmarks and then used OBGIM to induce stochastic resonance phenomena when solving difficult benchmark problems. Besides, they proposed a novel activation function based on the bistable SR echo state network (ESN) in [10], which replaces the tanh activation function representing the traditional threshold activation function, enhancing the noise adaptability of ESN.

However, the above-mentioned image enhancement methods mostly deal with noise or contrast in isolation. Moreover, the methods proposed in [11–13] only consider pixel-level processing and overlook the biological visual system. Although several image enhancement methods have been proposed, few consider the physiological mechanisms of human visual perception. In fact, the biological visual system can efficiently and robustly extract key information and form clear perceptions in extremely complex and dynamic natural scenes, whereas traditional methods often

perform well only under specific conditions. Furthermore, traditional methods lack generalization ability when facing unforeseen complex scenarios (such as extremely low light, uneven illumination, or complex noise), which can easily result in artifacts, over-smoothing, or loss of details, among others. According to [14], the visual system has directional selectivity for the target of interest in visual signal processing and selectively ignores noise information. In addition, the various visual cells in the biological visual system combine to form an array of receptive fields, forming clusters of anisotropic sensitive neurons in different directions. These pay more attention to the features in specific regions of interest and form an excitation mechanism, at the same time generating inhibitory electrical pulse responses in other insignificant directions [15]. In the biological visual mechanism, the retina model enhances images through the fusion of classical receptive fields [16] and non-classical receptive fields [17], as well as visual features such as modulation direction, brightness, and contrast [18]. In fact, the biological visual system can intelligently enhance perceptually salient details (such as object edges and textures) while suppressing unimportant background fluctuations or noise, achieving a contrast enhancement that is more in line with human visual perception habits, avoiding the common issues of over-enhancement or under-enhancement found in traditional enhancement methods. Therefore, traditional image enhancement methods are relatively simple, ignoring the physiological mechanisms of human eye imaging, struggling to conduct image enhancement under adverse factors, especially in terms of ship imaging.

Therefore, this article uses noisy ship images with low grayscale and contrast to simulate dim lighting environments as experimental objects and proposes a method for simulating biological visual imaging to improve image quality. The contributions of this proposed method are summarized as follows:

a) The proposed method takes the neuronal pulse emission mechanism and the directional selectivity of biological vision into account and takes advantage of the characteristics of random resonance of neurons. This makes the model consistent with the physiological characteristics of real visual imaging.

b) The stochastic resonance system converts noisy signals into useful signals and improves the quality of useful signals. A single neuron has stochastic resonance, but its processing ability is weak. Therefore, this paper constructs and concatenates a stochastic resonance system to significantly enhance its signal enhancement ability.

c) Contrast experiments are carried out based on the low-exposure and noisy ship images. Experimental results show that the proposed method performs better than the others in terms of PSNR and VIF, meaning that it can effectively enhance the visual brightness of the image and effectively remove the noise.

The remainder of this paper is organized as follows: The dual visual pathway receptive field model is presented in Section 2. The details of the proposed method are formally presented in Section 3. Section 4 gives the experimental results regarding the properties of our method. The conclusion is given in Section 5.

2. Dual visual pathway receptive field system model

2.1. Improved leaky integrate-and-fire (LIF) neuron model

The LIF neuron is a nonlinear excitable neural model that simulates the pulse emission generated by the stimulation of the axon of a nerve cell [19]; it can be equivalent to a capacitive-resistive circuit.

This model is used to describe the threshold membrane voltage discharge phenomenon of neuronal electrical pulses and to generate the physiological characteristics of electrical pulses under the continuous stimulation of external current. In other words, LIF simulates the dynamic changes of membrane potential and the pulse emission process of biological neurons. Specifically, when the presynaptic junction of a neuron is exposed to nerve current stimulation, an integrated membrane potential is formed. When the potential accumulation reaches a certain threshold, the neuron emits an action potential (a pulse), and then the potential resets. The frequency at which a neuron emits these action potentials can vary depending on the strength and duration of the input signal. When no external signals are received, the membrane potential gradually leaks to the resting potential. If we construct a suprathreshold LIF neuron model, the specific mathematical model can be given by

$$\begin{cases} \tau_m \dfrac{dv(x,y)}{dt} = -(v(x,y) - v_{reset}) + I(x,y) \\ v(x,y) = \begin{cases} 1, v(x,y) \geq v_{th} \\ 0, v(x,y) < v_{th} \end{cases} \end{cases} \tag{1}$$

where τ_m is the membrane capacitance time parameter playing a role in regulating the ignition rate, $v(x,y)$ is the neuronal integrated membrane potential, $I(x,y)$ is the input current excitation, v_{reset} denotes the resting membrane potential, and v_{th} is the pulse emission threshold. In fact, the traditional LIF responds to the pulse frequency, while a threshold is set above the threshold to obtain the emission count in the improved LIF. A suprathreshold neuron is a neuron that can generate an action potential (nerve impulse). When the change in its membrane potential reaches or exceeds the threshold potential, it triggers an all-or-none action potential. The intensity of the stimulus is encoded by the frequency (rather than the amplitude) of the action potential. The neurons integrate multiple inputs through synapses and trigger an action potential when the sum reaches a threshold. Then, the action potential is transmitted to the synaptic terminal, triggering the release of neurotransmitters and influencing the next neuron or effector. Since the axons of biological visual neurons have a cumulative nonlinear superposition effect on external stimuli, a potential well difference is generated on the cell membrane when a certain cumulative threshold is reached. On one hand, when the cumulative threshold is reached, pulses are emitted, which is similar to the way in which voltage is encoded in a single neuron. On the other hand, if the cumulative value is lower than the threshold, no pulses are generated. Therefore, the LIF neuron model is discretized and can be further described in units of time. Then, the discrete pulse emission is represented as

$$\begin{cases} h_t = f(v(x,y)_{t-1}, I(x,y)_t) = v(x,y)_{t-1} + \\ \dfrac{1}{\tau_m}(-v(x,y)_{t-1} + v_{reset} + I(x,y)_t) \\ s_t = \theta(h_t - v_{th}) \\ v_t = \begin{cases} 1, v(x,y) \geq v_{th} \\ 0, v(x,y) < v_{th} \end{cases} \end{cases} \tag{2}$$

where h_t represents the integrated membrane potential accumulated per unit time, v_t is the membrane potential of the neuron after the trigger pulse, θ is a step function, and s_t represents the pulse at time (which is 1 if a pulse is generated, otherwise 0). By Eq (2), the image can be discretely converted into an electrical pulse signal through neural nonlinear pulse coding. This is a conversion mode that conforms to the electrical stimulation generated by visual nerve cells when stimulated by

external light.

Figure 1 illustrates the encoding principle of the spike pulse sequence of neurons. In Figure 1(a), the orange curve represents different input current intensities, and the blue curve represents the action membrane potential and firing frequency of neurons. As seen from Figure 1(a), when the current exceeds the threshold of 1 and accumulates over time to reach the threshold voltage, a pulse is generated. If the current intensity is continuously greater than 1, the neuron continues to fire pulses. Otherwise, continuous firing will not be carried out. Besides, the intensity of the current determines the frequency of neuronal pulse firing. Figure 1(b) shows a sequence diagram of spike pulses corresponding to a single neuron. Figure 1(c) shows a sequence diagram of spike pulses generated by 100 neurons based on a random current sequence. As seen from Figure 1(a), the current pulses in the red box, the mutation signals, do not cause a sudden response to the pulse firing of neurons, which indicates that the neurons have the characteristics of damping and noise resistance in converting into pulse firing frequency. Based on this, noise interference can be effectively removed from the mutation signals. Since noise is a mutation index for images, converting the current signal of images into the encoded form of spike pulse firing of neurons has a certain smoothing effect.

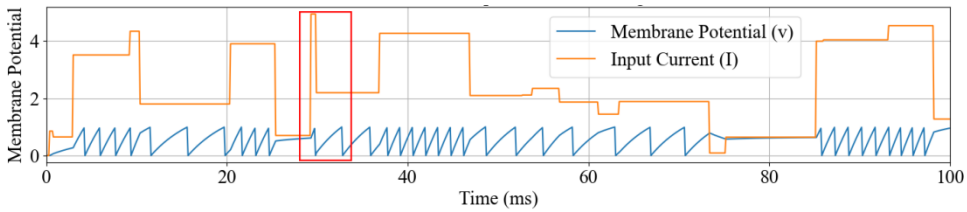

(a) Membrane potential and input current of a single neuron.

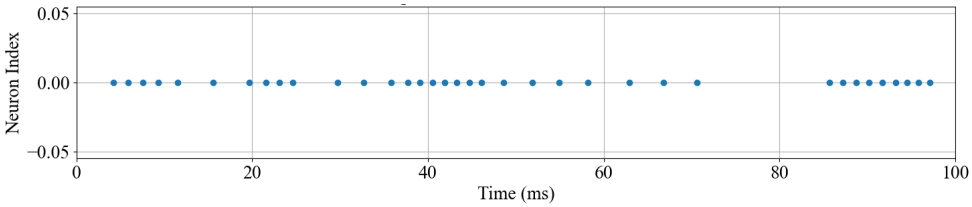

(b) Spike raster plot of a single neuron.

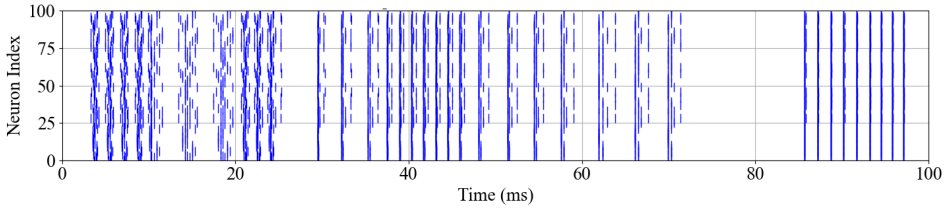

(c) Spike raster plot of 100 neurons.

Figure 1. Coding of neuronal spike pulse sequence.

2.2. Receptive fields in the dual visual pathways

In [20], Perona et. al. described the anisotropic diffusion equation, which has the characteristics of the visual direction mechanism due to its unique directional partial differential characteristics, expressed as

$$\begin{cases} \dfrac{\partial u(x,y,t)}{\partial t} = div(c(|\nabla u|)\nabla u, & t>0 \\ u(x,y,0) = u_0(x,y), & t=0 \end{cases}, \tag{3}$$

where $u_0(x,y)$ represents the input image, div represents the divergence operator, $c(|\nabla u|)$ is the diffusion coefficient function, t represents the scale factor, $|\nabla u|$ is the image gradient modulus function, and $c(|\nabla u|)$ is a nonnegative monotonic function of $|\nabla u|$. Usually, $c(x) = k^2/(x^2+k^2)$ or $c(x) = \exp(-(x^2/k^2))$, where k is a constant indicating the rate of decrease. The local diffusion coefficient $c(|\nabla u|)$ has different directional characteristics depending on the set function.

The partial differential equation image denoising method can remove image noise while maintaining image details such as edges and textures, but it will produce a staircase effect in the smooth area of the image. Although it considers the difference between the surrounding elements and the central elements, the direction selection characteristics of the human visual system and the visual physiological characteristics of the neuronal potential pulse emission are both ignored. In consequence, its image denoising results usually struggle to meet the requirements of being consistent with human subjective evaluation.

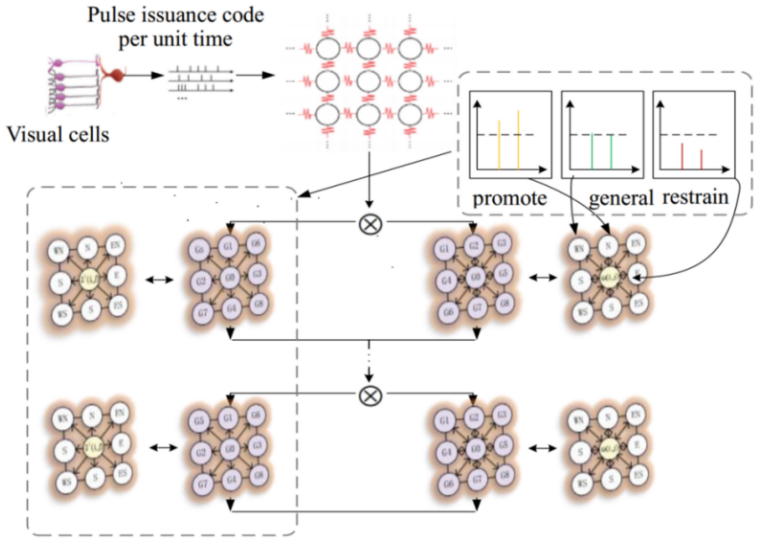

Figure 2. Dual visual pathway receptive field model.

According to research on the dual visual pathway, the upper pathway is mainly responsible for processing the fine information features of external visual stimuli [21], while the lower pathway is mainly responsible for processing coarse information [22]. Therefore, according to the information processing of the dual-channel dual-viewing pathway in [23], two fine and coarse image processing channels are constructed to perform directional filtering on the neural pulse encoding; also, a dual-viewing pathway receptive field model is constructed as shown in Figure 2 to conform to the image denoising mechanism of visual physiological characteristics.

Construct the diffusion coefficient function, normalize the image $I(i,j)$, and construct the retinal brightness calculation model within the receptive field, expressed as

$$\begin{cases} A(x,y) = \dfrac{\sum\limits_{(x_i,y_j)\in S_{x,y}} \tau(x_i,y_j) I(x_i,y_j)}{\sum\limits_{(x_i,y_j)\in S_{x,y}} \tau(x_i,y_j)} & (x_i \in [x-r,x+r],\ y_j \in [x-r,x+r]) \\ \tau(x_i,y_j) = 0.5\left[\cos\left(\dfrac{\pi}{r}\sqrt{(x_i-x)^2+(y_j-y)^2}\right)+1\right] \end{cases} \tag{4}$$

where $A(x,y)$ is the brightness model, $S_{x,y}$ is a square window with (x,y) as the center and d as the window length, $r=(d-1)/2$ is one half of the window length, and (x_i,y_j) is the window element from top to bottom and from left to right of the local window from the center pixel. Setting the directional response coefficient is given by

$$\delta^2(i,j) = \frac{1}{9}\sum_{i=i-1}^{i+1}\sum_{j=j-1}^{j+1}[I(i,j)-A(i,j)]^2 . \tag{5}$$

When the image is not contaminated by noise, the direction of the pixel area has greater correlation and continuity, the directional response coefficient of each pixel point is close to the pixel gray value, and the local variance is very small. However, for the isolated noise points, the changes in the eight directions are abrupt, the mean value of the pixels around them is quite different, and the local variance is relatively large. Taking this characteristic into consideration, the directional response coefficient will increase when noise appears in edge information or smooth continuous areas. Therefore, in this case, the local reaction coefficient can no longer effectively process the details accurately. For this reason, the diffusion coefficient function is reconstructed, and the substitution function is used to replace the central value based on the statistical mean replacement algorithm. Set the absolute value of the difference between the eight directions and the center point, shown as

$$R(i,j,\theta) = |f(i\pm1,j\pm1) - f(i,j)| \ (\theta = 0^\circ \sim 315^\circ). \tag{6}$$

The replacement function is shown as

$$\omega(i,j) = \arg(\text{average}\{\delta\sum_{x=i-1}^{i+1}\sum_{x=j-1}^{j+1}[R(i,j,\theta)]\}\Theta f(i,j)) \tag{7}$$

where δ represents the statistical difference, and Θ represents the corresponding pixel eight direction difference statistical average value replacement center value function. The diffusion coefficient function of the local variance is

$$c_1(|\nabla f(i,j)|) = \exp[-\delta(i,j)^2 \cdot |\nabla f(i,j)|]. \tag{8}$$

Another diffusion coefficient substitution function is

$$c_2(|\nabla f(i,j)|) = \omega(i,j) * f(i,j). \tag{9}$$

In summary, these two diffusion coefficient functions construct the anisotropic diffusion equation receptive field model of the bidirectional selection adaptive filter, which is shown as

$$\begin{cases} \dfrac{\partial u(x,y,t)}{\partial t} = \mu_1 div(c_1(|\nabla u|)\nabla u + \mu_2 div(c_2(|\nabla u|)\nabla u, \ t > 0 \\ u(x,y,0) = u_0(x,y), \ \ t = 0 \end{cases} \tag{10}$$

where $u_0(x,y)$ represents the original input image, div represents the divergence operator, t represents the scale factor, $|\nabla u|$ is the image gradient modulus function, c_1 is the local variance diffusion coefficient function, c_2 represents the diffusion coefficient function of the substitute function, μ_1 and μ_2 represent the coefficients of the selected diffusion coefficient function with the values of 0 or 1, and the sum is 1. The threshold of the difference between the center point value and the mean value of the eight directions is 0.2. If it is less than 0.2, the local variance is selected; otherwise, the substitute function is selected as the coefficient function. With consideration of the eight-neighborhood spatial relationship around the pixel point, the discretization iteration form is given by

$$f(i,j)^{t+1} = f(i,j)^t + \lambda[\sum_{m=1}^{8} cG_m \nabla G_m f(i,j)]^t \tag{11}$$

where G_m is the symbol representing the eight directions with the characteristic of direction selection, and c represents the diffusion coefficient function. The two diffusion functions in Eq (10) are selected according to the mean of the receptive field. m is an integer in the range of 1 to 8, $G_1 - G_4$ represent the four vertical and horizontal directions N, W, E, and S, respectively, and $G_5 - G_8$ represent the four diagonal directions WN, EN, WS, and ES, respectively. In order to ensure the stability of iteration, the condition of $0 \le \lambda \le 0.25$ is met.

3. Ship image enhancement method based on multi-scale spiking neural networks

The retina is composed of a large number of photoreceptor cells, which perform photoelectric conversion after being stimulated by light signals [24]. When the light intensity reaches a certain threshold, the neural electrical pulses are generated. After primary modulation by retinal cells, the signal is sent to the second layer for modulation processing. Then, the output is sent to the higher-level thalamo cortex for further processing, and stochastic resonance denoising occurs. These signals are transmitted to the cerebral cortex, where the contrast adaptive regulation occurs in the V1 and V2 pathways of the primary cerebral cortex, and the receptive field has a specific directional sensitivity to visual stimuli. Therefore, based on simulating the existence of the stochastic resonance mechanism and the specific modulation of visual brightness direction in visual pathway neurons, an image enhancement method that significantly improves visual communication is proposed.

3.1. Two-dimensional multiscale wavelet transform

An image can be regarded as a binary function, and its two-dimensional wavelet transform is defined as

$$W_j^{\lambda} f(x,y) = f * \psi_j^{\lambda}(x,y) = \iint_{R^2} f(u,v)\psi_j^{\lambda}(x-u, y-v)dudv \tag{12}$$

where λ represents the frequency components of three different scales, and j represents the scale

decomposition. The filter coefficient matrices corresponding to the wavelet function $\psi(x)$ and the scale function $\varphi(x)$ are set to $\mathbf{G}$ and $\mathbf{H}$, respectively, and the original image $f(x,y)$ is set to $\mathbf{C}_0$. Then, the two-dimensional wavelet decomposition can be expressed as

$$\begin{cases} \mathbf{C}_{j+1} = \mathbf{H}\mathbf{C}_j\mathbf{H}^* \\ \mathbf{D}_{j+1}^h = \mathbf{G}\mathbf{C}_j\mathbf{H}^* \\ \mathbf{D}_{j+1}^v = \mathbf{H}\mathbf{C}_j\mathbf{G}^* \\ \mathbf{D}_{j+1}^d = \mathbf{G}\mathbf{C}_j\mathbf{G}^* \end{cases} (j = 0, 1, \cdots, J-1) \tag{13}$$

where h, d, v represents the horizontal, diagonal, and vertical components, respectively. $\mathbf{H}^*$ and $\mathbf{G}^*$ represent the conjugate transposed matrix of $\mathbf{H}$ and $\mathbf{G}$. The corresponding wavelet reconstruction is described as

$$\mathbf{C}_{j\text{-}1} = \mathbf{H}^*\mathbf{C}_j\mathbf{H} + \mathbf{G}^*\mathbf{D}_j^h\mathbf{H} + \mathbf{H}^*\mathbf{D}_j^v\mathbf{G} + \mathbf{G}^*\mathbf{D}_j^d\mathbf{G} \quad (j = J, J-1, \cdots, 1) \tag{14}$$

where J represents the number of decomposition scale levels. According to the principle that image decomposition reduces pixels by half [25], if the image size is $M \times N$, the maximum number of decomposition layers is $\log_2 N$. Here, the image is decomposed into three layers by the discrete wavelet transform, and the decomposition coefficients of the image are LL_3, LH_n, HL_n, and HH_n with $n = 1, 2, 3$, respectively. LL_3 represents the lowest frequency component, which is a low-resolution (coarse-scale) approximation of the image, HL_n represents the horizontal high-frequency and vertical low-frequency components, LH_n represents the horizontal low-frequency and vertical high-frequency components, and HH_n represents the diagonal high-frequency component.

3.2. Parallel-series FitzHugh–Nagumo (FHN) stochastic resonance model

According to [26], the visual scene's current information is transmitted through neuronal axons, and a single neuron exhibits a stochastic resonance phenomenon. Here, the FHN neurons are chosen as the component unit of the stochastic resonance system [27]. The mathematical model of the FHN neuron is given by

$$\begin{cases} \varepsilon \dfrac{du}{dv} = u(u-a)(1-u) - v + A_T + I_{ext} \\ \dfrac{dv}{dt} = \gamma(u - v - b) \end{cases} \tag{15}$$

where u is the fast-changing membrane voltage variable, and v is the slow-changing recovery voltage variable. $\varepsilon(0 < \varepsilon < 1)$ and $\gamma(0 < \gamma < 1)$ represent the time constant, which plays a role in regulating the ignition rate. A_T is the critical value, a and b are constants of the equation group, and I_{ext} is the external current stimulus. Stochastic resonance has the ability to convert noise signals into useful signals. Since the signal processing effect of a single neuron in a strong noise background is not ideal, a bistable model is built and connected in series. The model is shown in Figure 3. The single bistable model corresponding to the block diagram can be described by

$$\frac{d^2u_{1i}}{dt^2} = \gamma / \varepsilon(u_{1i} - v_{1i} - b)[u_{1i}(u_{1i} - a)(1 - u_{1i}) - v_{1i} + A_r + I_{in}] \ (i = 1, 2, ...n) \tag{16}$$

$$\frac{d^2u_{2i}}{dt^2} = \gamma / \varepsilon(u_{2i} - v_{2i} - b)[u_{2i}(u_{2i} - a)(1 - u_{2i}) - v_{2i} + A_r + u_{j-1}] \ (j = 1, 2, ...m) \tag{17}$$

where m is the number of parallel connections, n is the number of series connections, and I_{in} is the input of the parallel part. In order to obtain better results, m and n are usually set to 2 and 4, respectively.

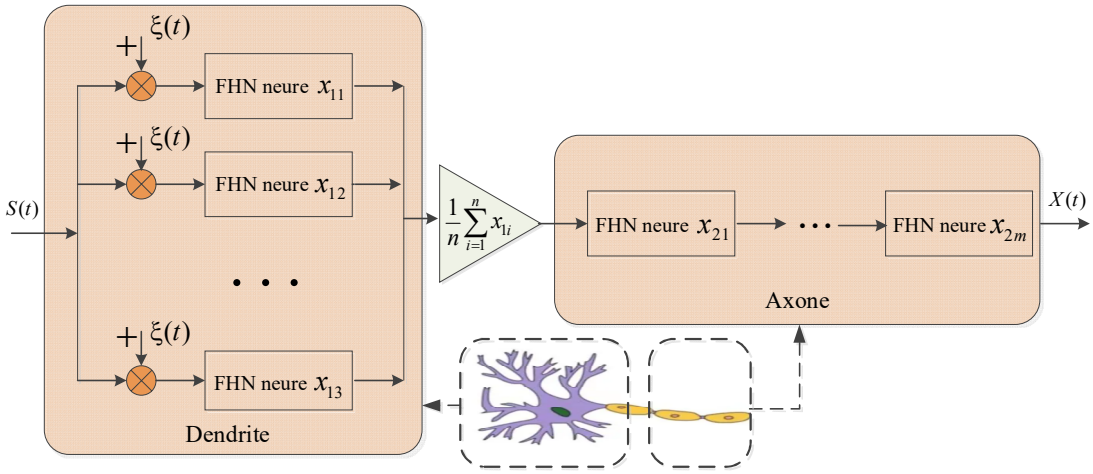

Figure 3. Parallel series FHN stochastic resonance model.

In fact, the FHN neuron has the characteristic of stochastic resonance and can convert noisy signals into useful signals, thereby enhancing the signal and removing the noise. In order to verify it, Figure 4 shows the effect diagrams of a single FHN neuron's stochastic resonance processing of one-dimensional aperiodic signals, with the different intensities of additive noise (D = 0.1, D = 0.5, and D = 1). Besides, Figure 5 shows the effect diagrams of stochastic resonance processing of one-dimensional aperiodic signals by two-stage parallel FHN neurons, also with D = 0.1, D = 0.5, and D = 1. It can be seen from Figure 4 that a single FHN has a certain denoising effect, but the denoising ability of a single FHN is relatively weak, and the effect is not satisfactory as the noise intensity increases. Compared with Figure 4, Figure 5 has a significant advantage in the denoising effect under the same intensity of additive noise and remains robust as the noise intensity increases.

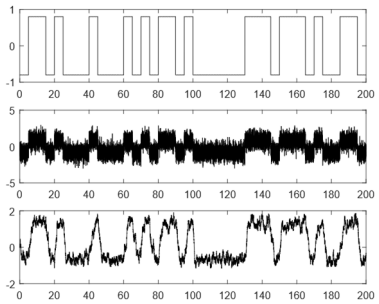

(a) D = 0.1

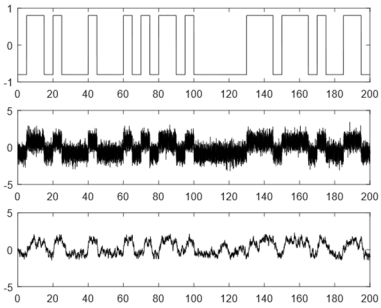

(b) D = 0.5

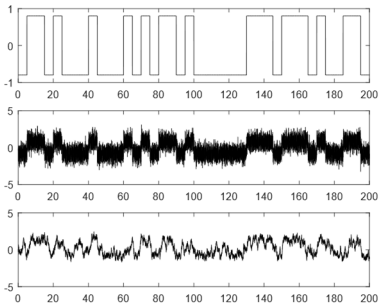

(c) D = 1

Figure 4. Comparison of stochastic resonance characteristics of a single FHN neuron.

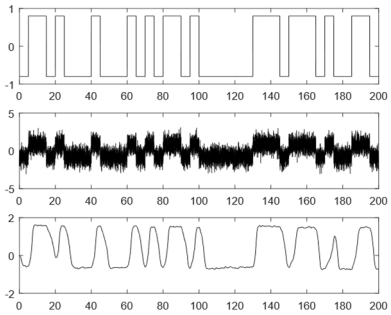

(a) D = 0.1

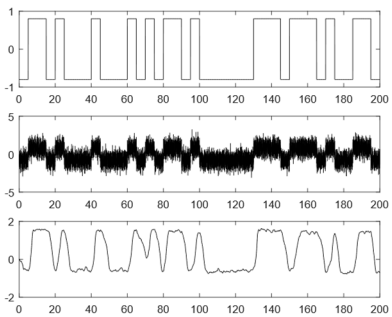

(b) D = 0.5

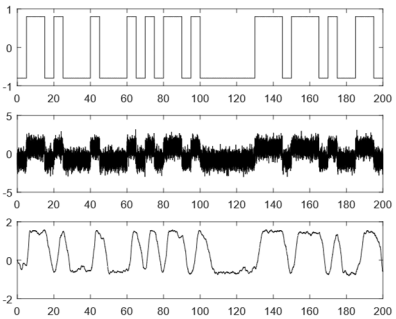

(c) D = 1

Figure 5. Comparison of stochastic resonance characteristics of two-stage parallel FHN neurons.

3.3. Algorithm flowchart

The algorithm flowchart is shown in Figure 6, and the specific operation steps of the algorithm are as follows.

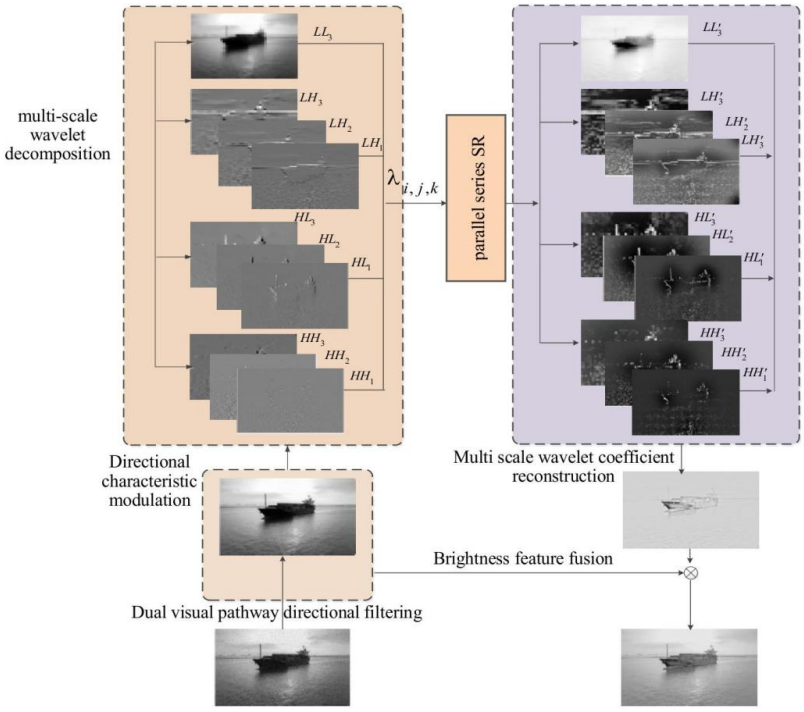

Figure 6. Algorithm flowchart.

a) The image $I(i,j)\,(i=1,2,\cdots M;\ j=1,2,\cdots N$, variables i and j are the same in the latter) in the field of view is normalized, $I(i,j)=S(t)+\xi(t)$, $S(t)$ is the input signal, and $\xi(t)$ is the Gaussian white noise. Then, the expression of the normalized image is shown as

$$f(i,j)=\frac{I(i,j)}{\max\left(I(i,j)\right)}(i=1,2,\cdots M \text{ and } j=1,2,\cdots N) \tag{18}$$

where $I(i,j)$ is the original noisy image, $\max(I(i,j))$ represents the maximum value of $I(i,j)$, M is the number of rows in the image, and N is the number of columns in the image.

b) The normalized image $M\times N$ is pulse-excited by an improved LIF neuron, the number of suprathreshold pulses is counted, and the statistical value is used as a nonlinear mapping code to obtain the matrix $g(x,y)$.

c) The diffusion coefficient of the binocular visual pathway receptive field model with a direction selection mechanism is constructed for primary denoising filtering, and the pulse-coded signal $g(x,y)$ is spatially convolution filtered. The local directional response coefficient and the substitution function are automatically selected according to the difference between the current central value and the surrounding eight directions. Besides, the matrix $h(x,y)$ is obtained after binocular visual pathway modulation.

d) The signal $h(x,y)$ of the primary modulation of the neural pulse coding of the dual visual pathway

is decomposed into a three-level two-dimensional wavelet. Since the low-frequency signal is the main image information and the high-frequency signal contains noise, the coefficients of wavelet decomposition need to be adjusted. In order to improve the quality of the nonlinear stochastic resonance output signal, the shrinkage factor λ_{ijk} is introduced for each frequency component to adjust the amplitude of each scale component. λ_{ijk} is defined as

$$\lambda_{ijk} = \beta\sigma_n\left(\frac{1}{1+e^{-(i+j+k)}}\right)\left(\frac{\sigma(A)}{\sigma(|A|)}\right)^2 (i=1,2; j=1,2; k=1,2,3) \tag{19}$$

where σ_n is the standard deviation of the noise, 1 represents L, and 2 represents H. A represents the scale frequency coefficient set. β is the adjustment coefficient. The one-dimensional signal $p_{ij}(n)(n=1,2,...,M_i \times N_i; i=1,2,...,10; j=1,2,...,4)$, obtained by processing the wavelet coefficient matrices of different scales, is sent into the series-parallel FHN stochastic resonance system after shrinkage factor processing, for obtaining the coefficient-enhanced signal $x_i(t)(i=1,2,...,10)$.

e) Then, the coefficient matrix $x(t)$ after series-parallel processing is subjected to the inverse wavelet transform to obtain the final output matrix $u(x,y)(x=1,2,...,M; y=1,2,...,N)$.

f) Considering the characteristic of photometric feature adjustment in the visual path system, the coefficient matrices $u(x,y)$ and $h(x,y)$, reconstructed by wavelet inverse transform, are finally fused with point pixel mean values. In order to obtain the best output, the coefficients a and b of $a \cdot u(i,j)$ and $b \cdot h(i,j)$ are used as the optimization parameters, and the visual information fidelity VIF in Eq (22) is used as the fitness function. The quantum particle swarm algorithm [28] is used to find the optimal parameters for obtaining the final enhanced image, and the fusion processing result of the dual-view pathway model output and the multi-scale wavelet coefficient brightness mean is shown as

$$o(i,j) = \frac{au(i,j) + bh(i,j)}{a+b} (i=1,2,\cdots M; j=1,2,\cdots N) \tag{20}$$

4. Experimental results and analysis

The software used for this article is MATLAB 2016b. The experimental images were obtained from public data on the Internet, and the shooting environment was selected from a rainy and dark weather scene to obtain a grayscale image with low light. Figure 7 gives the original image of the ship.

Figure 7. Original ship image.

4.1. Process analysis of the proposed method

This section provides a detailed description of each process of the entire algorithm flowchart of Figure 6. Considering that the dual visual pathway serves as the primary cerebral cortex, it can simulate preprocessing and conduct preliminary processing on Figure 8(a) (i.e., the noisy image with the corresponding noise intensity D = 0.01, simulating a mixed low-quality noisy image signal) for obtaining Figure 8(b). Compared with Figure 8(a), in Figure 8(b), the noise was preprocessed better. Figure 8(c) shows the processing results of multi-scale wavelet decomposition, which divides the signal into high and low frequencies and further processes the signals in different frequency domains in order to further denoise and increase contrast. Figure 8(d) shows the processing results of the two-stage stochastic resonance. Compared with Figure 8(c), it can be seen that the contrast between high and low frequencies has increased. Figure 8(e) is the result of performing inverse wavelet transform on Figure 8(d). It can be seen that the brightness has been significantly enhanced, but it still needs to be adjusted through the brightness system in the visual system. When Figure 8(e) is fused with the result of the dual visual pathway (brightness), the fusion result is as shown in Figure 8(f). According to the entire process, each visual module has a corresponding function, which can be reflected from the figure and is also in line with the theory of the proposed model. Eventually, the final result has a better improvement effect compared to the original image.

(a) Figure 7 with noise intensity D = 0.01

(b) Result of dual-view pathway receptive field

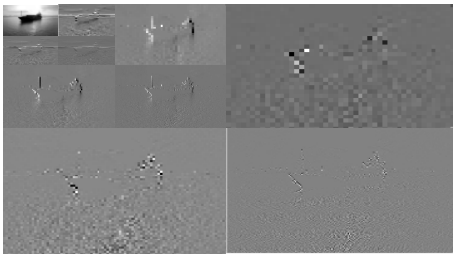

(c) Results of multi-scale wavelet decomposition

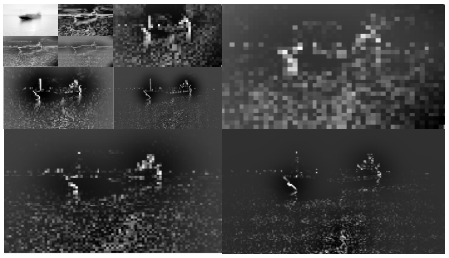

(d) Results of two-stage stochastic resonance

(e) Multi-SR processing result

(f) Fusion result

Figure 8. Diagrams for different processing stages of the proposed method.

4.2. Objective evaluation

Histogram statistics are an intuitive display method of significance for the distribution of image pixels and can objectively analyze the brightness distribution of pixels. The images in Figure 8(b), Figure 8(e), and Figure 8(f) are displayed intuitively by histograms, and the results are shown in Figure 9.

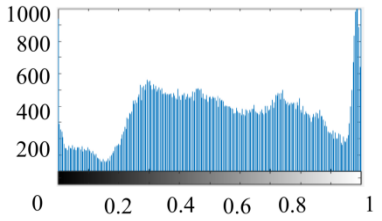

(a) Dual-view channel filtering histogram

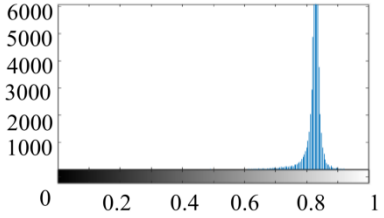

(b) Multi-SR processing histogram

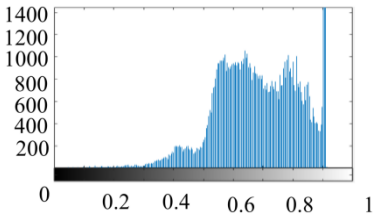

(c) Fusion histogram

Figure 9. Histograms corresponding to Figure 8.

As seen from Figure 9, although the pixel distribution in Figure 9(a) is relatively balanced, there are more dark pixels overall. Figure 9(b) shows that most of the pixels are concentrated around 0.8, indicating that energy migration has occurred through random resonance in the wavelet frequency domain, and the overall pixel brightness is high. Figure 9(c) is the result of brightness feature modulation after the fusion of Figure 9(a),(b). The energy is neutralized by negative feedback modulation. The overall pixel distribution is above 0.5, and the pixel distribution is relatively balanced, which is visually brighter.

Since the perceptual quality matrix (PQM) can skillfully evade the reference images and the variance (Var) can reflect the heterogeneity among all the pixels, the PQM and Var are chosen as the evaluation indicators, as in [29]. According to [29], the closer PQM is to 10, the better the quality of the image. Besides, the variance shows low contrast when the overall value is darker or brighter, and the variance value actually decreases. When the contrast of pixel step values with different gradients increases, the variance value shows a higher value. In order to further verify the superiority of the proposed method, three ship images of the same type of scene are shown in Figure 10. The noisy images with added noise intensity D = 0.01 to the original image are shown in Figure 10(a), the results of being processed by the multi-scale pulse neural network stochastic resonance system are shown in Figure 10(b), and the final fused effect images are given in Figure 10(c). Finally, Figure 10(d) gives the indicator graph of variance and PQM presented with noise intensity, where the red variance curve shows that the best performance is achieved when the noise intensity is around 0.3. Besides, the blue

curve of PQM reaches its peak for obtaining the optimal indicator parameters when the noise intensity is also around 0.3.

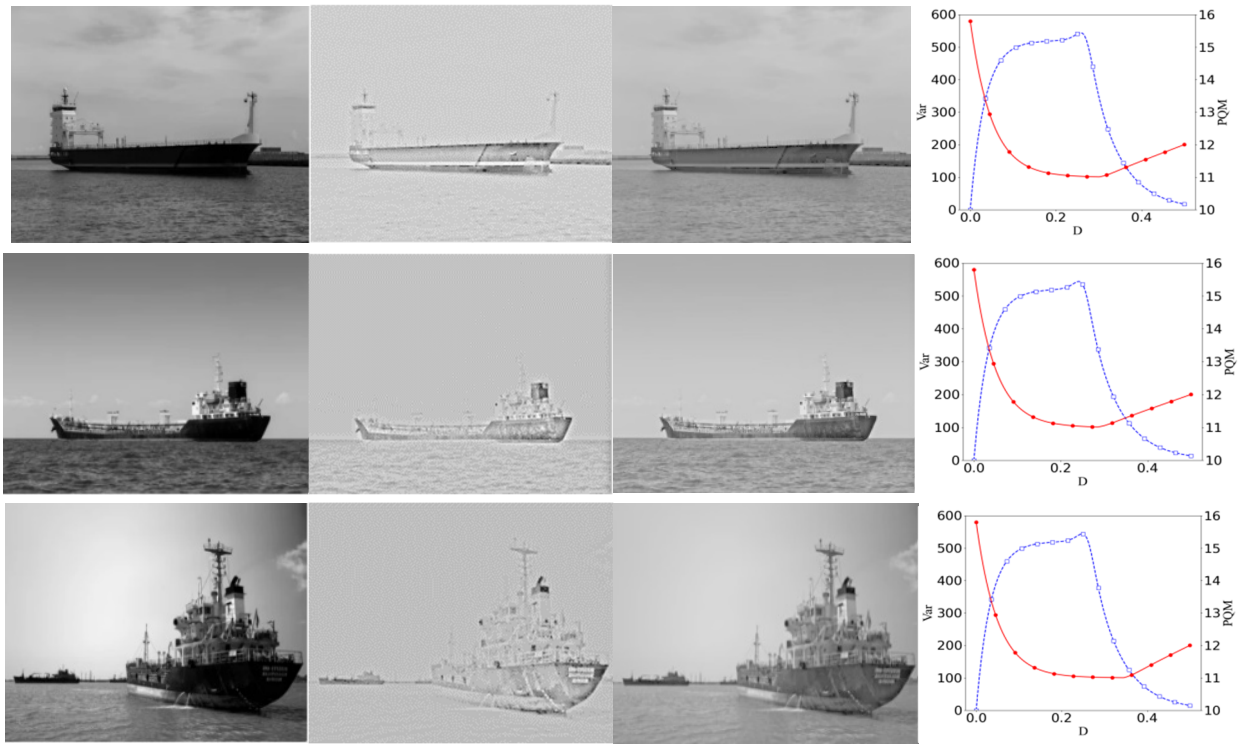

(a) Original Image (b) Multi-SR processing effect (c) Fusion image (d) PQM and Var Indexes

Figure 10. Image processing rendering of the ship section.

To further demonstrate the generalization of the proposed method, 12 sets of ship images of the same class are selected for testing. The dataset is shown in Figure 11 and is named a-l in alphabetical order from top to bottom and left to right. The noise intensity is enhanced by D = 0.01, and PSNR and VIF are selected as evaluation indicators, as shown in Table 1.

Figure 11. Twelve sets of ship diagrams of the same type (from image a to l).

Table 1. Comparisons of original and enhanced images.

Original image	Noisy image		Proposed method	
	PSNR	VIF	PSNR	VIF
a	9.7762	0.4256	12.4302	0.5022
b	9.7628	0.4285	12.3098	0.5455
c	9.7621	0.4328	12.3283	0.5234
d	9.1923	0.3762	12.0982	0.5983
e	9.3129	0.4209	12.0933	0.5423
f	9.7651	0.3342	12.9083	0.3983
g	9.5427	0.3783	12.5222	0.4234
h	9.6254	0.4763	12.9845	0.5033
i	9.2358	0.4023	12.3433	0.6512
j	9.9654	0.3982	12.0234	0.6055
k	9.0245	0.4897	12.4643	0.6093
l	9.6856	0.4322	12.6498	0.3902

To further verify that the proposed method has a good processing effect on low-contrast and noisy images, a contrast method is used for horizontal comparison. The proposed method is compared with MIMV [30], IET [31], CWTN [32], and EAIR [33]. The parameters of the proposed model are set to $\tau_m = 0.1$, $v_{reset} = -30$, and $v_{th} = 0.6$ for the LIF neuron model, and $A_T = 0.6$, $\varepsilon = 0.15$, and $\gamma = 0.8$ (representing time constant, which plays a regulating role in the ignition rate) for the FHN model; coefficients are $a = 0.2$ and $b = 0.3$. In the experiment, the first five diagrams in Figure 11 are selected. The comparison results of different algorithms are shown in Figure 12. The first row represents the five original images, and the second row illustrates the corresponding noisy images with additive noise with a mean of 0 and a standard deviation of noise intensity of 1; these are also the target images to be processed.

The MIMV method enhanced the low-contrast, noisy images by constructing the FHN neural network and then proposing a visual model. However, it ignored the characteristics of perceived wild objects in different pathways, the stochastic resonance array mechanism, and the harmonic effect of the luminance negative feedback adjustment pathway. The processing results show that although it can effectively enhance the brightness of the image, noise is still prominent. Besides, the contrast does not reflect the details of the layers, and the overall brightness is rather high. The IET method resulted in not much detail distortion, but the increase in brightness is relatively dim and mild. Compared with the above-mentioned methods, the CWTN method can effectively filter out most noise, enhance bright areas, and stretch contrast. Moreover, the number "174" can be easily seen in the red wireframe, which is much clearer than in the other methods. The EAIR method only considers the brightness factor and is relatively simple. Due to the influence of noise factors, while brightening, it causes more fogging and impurities in the figure. Through subjective visual examination of the images processed by the proposed method (OURS), it can be seen that while brightness is increased and the contrast is stretched, the details are well preserved without distortion. Besides, the noise in the background and target area is relatively well removed. The number "174" can be clearly distinguished with no blurring or other effects, even clearer than in CWTN. In summary, the proposed method can effectively enhance the contrast and brightness and suppress noise while preserving hierarchical details.

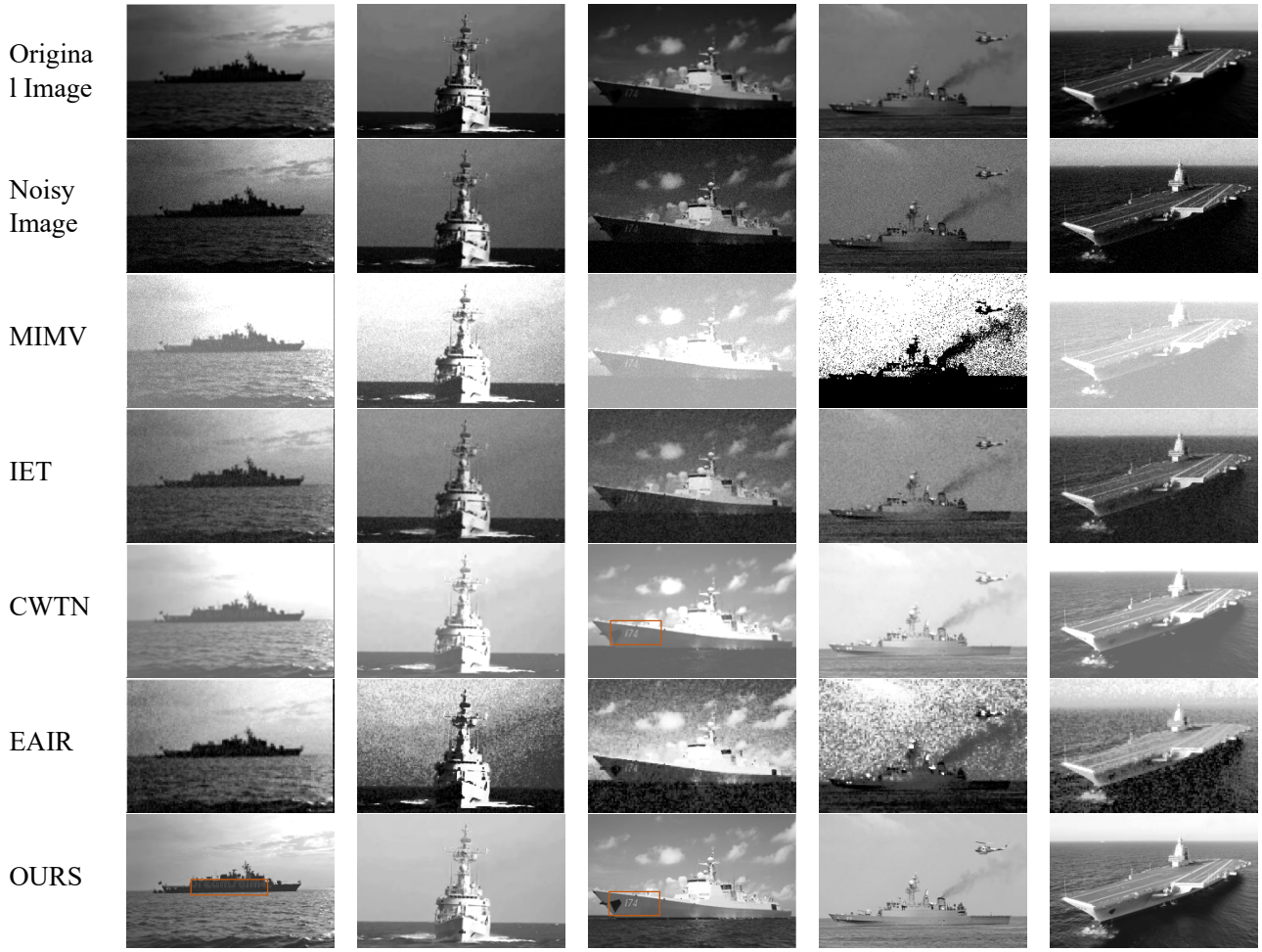

Figure 12. Processing results of ship diagrams of Figure 11(a–e) by different algorithms.

In this paper, the peak signal-to-noise ratio (PSNR) [34] and visual information fidelity (VIF) [35] are selected as image enhancement evaluation indicators. The principle of PSNR is to calculate the logarithmic value of the mean square error between the original image and the processed image, which is calculated by

$$\mathrm{PSNR} = 10\lg[\frac{(2^n-1)^2}{\mathrm{MSE}}]\ (\mathrm{db}) \tag{21}$$

where MSE (i.e., mean square error) between the original image and the processed image can be calculated by

$$\mathrm{MSE} = \frac{1}{MN}\sum_{(i,j)=1}^{M,N}(f^*(i,j)-f(i,j))^2 \tag{22}$$

where $f^*(i,j)$ and $f(i,j)$ represent the filtered image and the ideal image, respectively. The better the denoising effect, the smaller the MSE.

VIF is a natural image quality evaluation index based on a natural scene statistical model, image distortion, and human visual distortion modeling. The VIF index formula of visual information fidelity is

$$\mathrm{VIF}=\frac{\sum_{j\in M} I\left(\vec{C}^{N,j};\vec{F}^{N,j}\mid s^{N,j}\right)}{\sum_{j\in M} I\left(\vec{C}^{N,j};\vec{E}^{N,j}\mid s^{N,j}\right)} \tag{23}$$

where $\vec{C}^{N,j}$ is the number of N GMS models of the *j-th* sub-band of wavelet decomposition, and M is the number of sub-bands of wavelet decomposition. $\vec{E}$ and $\vec{F}$ are the visual outputs of the reference and distorted images after passing through the HVS model, respectively. The data analysis results of the extended image in Figure 10 are shown in Figure 13.

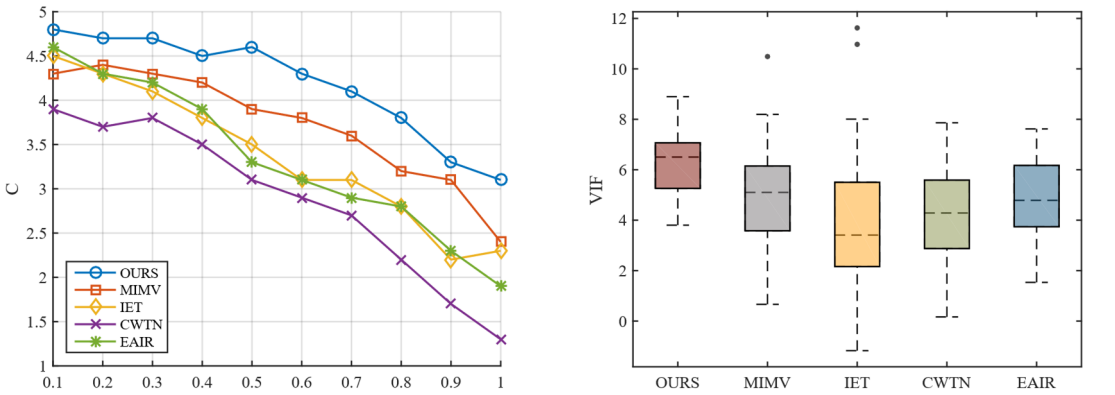

(a) PSNR corresponding to different noises

(b) VIF corresponding to different algorithms

Figure 13. Different methods for processing the corresponding PSNR.

Figure 13(a) shows the correlation curve between PSNR and noise intensity for the original ship in Figure 7 with different noise intensities. It can be seen from the curves that as the noise intensity increases, bilateral filtering, wavelet filtering, single neuron, and our method are used to process the PSNR curve. The performance curve of the proposed algorithm is relatively stable and slightly higher than that of the other algorithms, indicating good robustness and superiority in denoising. Twelve ship images of the same type are selected and compared for image quality using algorithms MIMV, IET, CWTN, and EAIR. VIF is used as the evaluation metric, as shown in Figure 13(b). Results show that the median value of the proposed method is slightly higher than that of the other algorithms, and the lower limit value also has certain advantages.

As seen from Table 1, compared with the mixed signal image mixed with noise, the PSNRs of these enhanced ship images are significantly improved by about 27%; also, their VIFs are objectively improved by about 30%. In fact, the VIF index is more consistent with the visual effect of human eyes, which is a quantitative way to judge image quality.

To further compare and analyze the image quality effects processed by different algorithms, the peak signal-to-noise ratio (PSNR) is adopted as the evaluation index, as shown in Table 2. Table 2 shows the original images in Figure 9 with additive noises of D = 0.1, 0.5, and 1. By comparing the values of PSNR processed by different algorithms, it can be seen that the reduction in PSNR of the proposed algorithm is relatively small, demonstrating good robustness in denoising and indicating that the quantitative indicator is also consistent with the visual subjective.

Table 2. Comparisons of PSNR by different algorithms.

Original image	Algorithm	PSNR		
		D = 0.1	D = 0.5	D = 1
a	MIMV	11.3349	9.7442	8.4452
	IET	12.0423	10.4434	9.7565
	CWTN	10.9866	8.9677	7.9676
	EAIR	12.1986	11.6568	10.6564
	OURS	12.7978	12.5565	12.1445
b	MIMV	11.0534	9.5453	8.3544
	IET	12.5665	10.0453	9.4545
	CWTN	10.7677	8.7674	7.8342
	EAIR	12.6342	10.5352	10.6564
	OURS	12.8465	12.4546	12.1456
c	MIMV	11.5766	9.5657	8.8567
	IET	11.9701	10.5678	9.7787
	CWTN	11.0678	8.7674	7.9885
	EAIR	12.7123	10.4554	10.7096
	OURS	12.6098	12.3775	12.2097
d	MIMV	11.0234	9.7442	8.7575
	IET	12.4466	10.4234	9.7765
	CWTN	10.9765	8.3988	7.9655
	EAIR	12.7875	10.9567	10.8567
	OURS	12.8787	12.2644	12.1245
e	MIMV	11.3676	9.8874	8.6456
	IET	12.7563	10.6785	9.8123
	CWTN	11.1344	8.6223	7.7542
	EAIR	12.2422	10.0422	10.9544
	OURS	12.6342	12.3234	12.2322

5. Conclusions

In this paper, the proposed method, which fuses the parallel-series stochastic resonance model and the multi-scale spiking neural network, can effectively enhance visual brightness, remove noise, highlight details, and eventually improve image recognition. Considering the neuron pulse emission coding mechanism and biological vision characteristics, the primary processing of the receptive field model is constructed, and the multi-scale wavelet and FHN parallel-series stochastic resonance model is constructed. The coefficients are reconstructed after the multi-scale wavelet coefficient stochastic resonance system is processed, and finally, brightness characteristics are considered for visual fusion. The proposed method considers the mechanism of neuronal pulse firing and the directional selectivity of biological vision, combined with the characteristic of random resonance of neurons, aligning it better with the physiological characteristics of real visual imaging and signal processing. Therefore, the proposed method has a relatively ideal image enhancement effect, which is critical in ship image enhancement. Though the proposed method in this paper has a relatively effective enhancement effect on low-contrast and noisy images, it still has certain limitations. For instance, the visual system model

mainly focuses on the preprocessing of the primary and intermediate visual cortices, which lacks the ability for in-depth image analysis and recognition. In the future, attempts can be made to model the advanced visual cortex and recognize and analyze low-quality images.

Use of AI tools declaration

The authors declare they have not used Artificial Intelligence (AI) tools in the creation of this article.

Acknowledgments

This work was supported in part by the High-level Talent Research Initiation Fund Project of Taizhou University under Grant TZXYQD2024A007 and the National Natural Science Foundation of China under Grant 12202427.

Conflict of interest

The authors declare there is no conflict of interest.

References

1. H. Li, X. L. Duan, SAR ship image speckle noise suppression algorithm based on adaptive bilateral filter, *Wireless Commun. Mobile Comput.*, **2022** (2022), 9392648. https://doi.org/10.1155/2022/9392648
2. X. Bai, F. Zhou, B. Xue, Infrared image enhancement through contrast enhancement by using multiscale new top-hat transform, *Infrared Phys. Technol.*, **54** (2011), 61–69. https://doi.org/10.1016/j.infrared.2010.12.001
3. J. C. M. Román, R. Escobar, F. Martínez, J. L. V. Noguera, H. Legal-Ayala, D. P. Pinto-Roa, Medical image enhancement with brightness and detail preserving using multiscale top-hat transform by reconstruction, *Electron. Notes Theor. Comput. Sci.*, **349** (2020), 69–80. https://doi.org/10.1016/j.entcs.2020.02.013
4. J. Pei, Z. Yu, J. Wu, Y. Zhao, X. Yang, Maritime infrared image enhancement based on morphological pseudo transmittance modulation and radiation source enhancement, *Infrared Phys. Technol.*, **142** (2024), 105564. https://doi.org/10.1016/j.infrared.2024.105564
5. L. Gammaitoni, P. Hänggi, P. Jung, F. Marchesoni, Stochastic resonance, *Rev. Mod. Phys.*, **70** (1998), 224–287. https://doi.org/10.1103/RevModPhys.70.223
6. Z. Shi, Z. Liao, H. Tabata, Enhancing performance of convolutional neural network-based epileptic electroencephalogram diagnosis by asymmetric stochastic resonance, *IEEE J. Biomed. Health. Inf.*, **27** (2023), 4228–4239. https://doi.org/10.1109/JBHI.2023.3282251
7. D. V. Dylov, J. W. Fleischer, Nonlinear self-filtering of noisy images via dynamical stochastic resonance, *Nat. Photonics*, **4** (2010), 323–328. https://doi.org/10.1038/nphoton.2010.31
8. Z. Liao, Z. Shi, H. Tabata, One-dimensional lattice potential-based stochastic resonance for robust QRS detection in noisy electrocardiogram, *IEEE Sens. J.*, **24** (2024), 35323–35332. https://doi.org/10.1109/JSEN.2024.3462799

9. Z. Liao, K. Ma, S. Sarker, H. Yamahara, M. Seki, H. Tabata, Overdamped Ising machine with stochastic resonance phenomena in large noise condition, *Nonlinear Dyn.*, **112** (2024), 8967–8984. https://doi.org/10.1007/s11071-024-09486-y
10. Z. Liao, Z. Wang, H. Yamahara, H. Tabata, Echo state network activation function based on bistable stochastic resonance, *Chaos, Solitons Fractals*, **153** (2021), 111503. https://doi.org/10.1016/j.chaos.2021.111503
11. L. Li, R. Wang, W. Wang, W. Gao, A low-light image enhancement method for both denoising and contrast enlarging, in *2015 IEEE International Conference on Image Processing (ICIP)*, (2015), 3730–3734. https://doi.org/10.1109/ICIP.2015.7351501
12. H. Ackar, A. Abd Almisreb, M. A. Saleh, A review on image enhancement techniques, *Southeast Eur. J. Soft Comput.*, **8** (2019), 42–48. http://doi.org/10.21533/scjournal.v8i1.175
13. W. Wang, X. Wu, X. Yuan, Z. Gao, An experiment-based review of low-light image enhancement methods, *IEEE Access*, **8** (2020), 87884–87917. http://doi.org/10.1109/ACCESS.2020.2992749
14. D. A. Tarzanagh, Y. Li, X. Zhang, S. Oymak, Max-margin token selection in attention mechanism, in *Proceedings of the 37th International Conference on Neural Information Processing Systems*, **36** (2023), 48314–48362.
15. Q. X. Wu, M. McGinnity, L. Maguire, A. Belatreche, B. Glackin, Edge detection based on spiking neural network model, in *Advanced Intelligent Computing Theories and Applications. With Aspects of Artificial Intelligence*, (2007), 26–34. https://doi.org/10.1007/978-3-540-74205-0_4
16. K. Ghosh, S. Sarkar, K.Bhaumik, Image enhancement by high-order Gaussian derivative filters simulating non-classical receptive fields in the human visual system, in *Pattern Recognition and Machine Intelligence*, (2005), 453–458. https://doi.org/10.1007/11590316_70
17. X. Du, Y. Cheng, Z. Gu, Non-classical receptive field models with inhibitory subunits for high-speed railway image enhancement, in *Proceedings of the 4th International Conference on Computer Science and Application Engineering*, (2020), 1–5. https://doi.org/10.1145/3424978.3425113
18. K. F. Yang, C. Y. Li, Y. J. Li, Multifeature-based surround inhibition improves contour detection in natural images, *IEEE Trans. Image Process.*, **23** (2014), 5020–5032. https://doi.org/10.1109/TIP.2014.2361210
19. J. K. Han, M. S. Kim, S. I. Kim, M. W. Lee, S. W. Lee, J. M. Yu, Investigation of leaky characteristic in a single-transistor-based leaky integrate-and-fire neuron, *IEEE Trans. Electron Devices*, **68** (2021), 5912–5915. https://doi.org/10.1109/TED.2021.3110830
20. Y. Chen, B. Paromita, On the incorporation of time-delay regularization into curvature-based diffusion, *J. Math. Imaging Vision*, **14** (2001), 149–164. https://doi.org/10.1023/A:1011211315825
21. J. J. DiCarlo, D. Zoccolan, N. C. Rust, How does the brain solve visual object recognition? *Neuron*, **73** (2012), 415–434. https://doi.org/10.1016/j.neuron.2012.01.010
22. J. E. LeDoux, The emotional brain: The mysterious underpinnings of emotional life, Simon & Schuster, 1996.
23. J. V. Stone, Vision and brain: How we perceive the world, MIT press, 2012. https://doi.org/10.1002/col.21807
24. H. Wassle, B. B. Boycott, Functional architecture of the mammalian retina, *Physiol. Rev.*, **71** (1991), 447–480. https://doi.org/10.1152/physrev.1991.71.2.447

25. S. C. Lo, H. Li, M. T. Freedman, Optimization of wavelet decomposition for image compression and feature preservation, *IEEE Trans. Med. Imaging*, **22** (2003), 1141–1151. https://doi.org/10.1109/TMI.2003.816953
26. A. Longtin, Stochastic resonance in neuron models, *J. Stat. Phys.*, **70** (1993), 309–327. https://doi.org/10.1007/BF01053970
27. Y. F. Guo, B. Xi, F. Wei, J. G. Tan, Stochastic resonance in FitzHugh-Nagumo neural system driven by correlated non-Gaussian noise and Gaussian noise, *Int. J. Mod. Phys. B*, **31** (2017), 1750264. https://doi.org/10.1142/S0217979217502642
28. W. Fang, J. Sun, Y. Ding, X. Wu, W. Xu, A review of quantum-behaved particle swarm optimization, *IETE Tech. Rev.*, **27** (2010), 336–348. https://doi.org/10.4103/0256-4602.64601
29. Y. Fu, Y. Kang, G. Chen, Stochastic resonance based visual perception using spiking neural networks, *Front. Comput. Neurosci.*, **14** (2020), 24. https://doi.org/10.3389/fncom.2020.00024
30. Z. Xu, Y. Zhai, Y. Kang, Mutual information measure of visual perception based on noisy spiking neural networks, *Front. Neurosci.*, **17** (2023), 1155362. https://doi.org/10.3389/fnins.2023.1155362
31. T. A. Soomro, M. Rathi, S. A. Soomro, M. U. Keerio, P. Kumar, E. N. Baro, Image enhancement technique for MRI brain images, in *2024 Global Conference on Wireless and Optical Technologies (GCWOT)*, (2024), 1–5. https://doi.org/10.1109/GCWOT63882.2024.10805684
32. X. Liu, T. D. Nguyen, Medical images enhancement by integrating CLAHE with wavelet transform and non-local means denoising, *Acad. J. Comput. Inf. Sci.*, **7** (2024), 52–58. https://doi.org/10.25236/AJCIS.2024.070108
33. Y. Zhang, T. Zhang, C. Liu, L. Zhang, Low light image enhancement algorithm based on improved retinex, in *2024 9th International Conference on Computer and Communication Systems (ICCCS)*, (2024), 184–189. https://doi.org/10.1109/ICCCS61882.2024.10602798
34. A. Tanchenko, Visual-PSNR measure of image quality, *J. Visual Commun. Image Represent.*, **25** (2014), 874–878. https://doi.org/10.1016/j.jvcir.2014.01.008
35. H. R. Sheikh, A. C. Bovik, Image information and visual quality, *IEEE Trans. Image Process.*, **15** (2006), 430–444. https://doi.org/10.1109/tip.2005.859378

AIMS Press